Stand-Alone Cosmic-Ray Tomography with Secondary Particles

Maximilian Pérez Prada, Sarah Barnes, and Maurice Stephan

German Aerospace Center (DLR), Institute for the Protection of Maritime Infrastructures, Fischkai 1, 27572 Bremerhaven, Germany

Corresponding author: Maximilian Pérez Prada
Email address: m.perezprada@dlr.de

Abstract

The imaging technique of cosmic-ray tomography is usually based on the measurement of muon transmission and muon scattering within the examined volume. Secondary particles produced from the interaction of air shower particles with the target material have been proven to carry complementary information directly related to the target material properties. However, this additional information has not been fully exploited so far. Previous work by the authors [Analysis of Secondary Particles as a Complement to Muon Scattering Measurements. *Instruments* 2022, 6] showed a novel approach utilizing only the information from secondary particles to successfully reconstruct and discriminate a variety of materials in the context of shipping container scanning with an optimal detector setup and background-free environment. This work builds on the previous results and methods, taking more realistic detector parameters into consideration and investigating their impact on material reconstruction and discrimination. A possible detector setup is discussed, allowing the reconstruction of muons and secondary particle tracks. Three key detector parameters are varied with the aim of validating the approach of the previous work in a more realistic scenario. These parameters are the detection efficiency, the spatial resolution, and the spacing between the detector layers.

1. INTRODUCTION

The field of nondestructive imaging, especially in the field of safety and security, is steadily evolving through new concepts and measurement methods. In recent years, cosmic-ray tomography has been proven to be a viable part of this technological arsenal [2, 3, 4, 5, 6, 7, 8, 9]. High-energy cosmic rays interact with the nuclei in the earth's atmosphere and create a cascade of energetic particles raining toward the earth's surface. These so-called air showers consist, among other particles, of muons, photons, neutrons, and electrons at sea level [10, 11, 12, 13].

Air shower muons mostly interact with atoms through Coulomb scattering, which, in combination with their mass, allows for a high material penetration depth, making them an ideal natural radiation source for nondestructive imaging. The resulting scattering angle is proportional to the atomic number and the density of the examined target, allowing for the reconstruction and discrimination between different materials and objects [14, 15]. Complementary to this technique of Muon Scattering Tomography, Muon Radiography utilizes the muon absorption rate, which is also dependent on the atomic number and density of the material [16, 17].

When air shower particles interact with surrounding matter, they lose energy in the form of additional photons, electrons, and neutrons, so-called secondary particles. The production rate and kinematics of these particles are related to the physical properties of the surrounding material [18, 19, 20, 21, 22, 23, 24, 25, 26], resulting in complementary information to the measurements obtained through Muon Scattering Tomography or Muon Radiography. Currently, the main approach to use this information is a measurement of secondary particles in coincidence with air shower muons [27, 28, 29, 30, 31]. However, previous work by the authors [1] introduced a novel technique solely relying on the measurement of secondary particles. Under an optimal detector setup and background-free environment, an analysis of the content in a shipping container was proven to be feasible.

This work takes the prior proof of concept study and expands the scope to include more realistic detector conditions. Therefore, this work focuses on the implementation of realistic detector parameters and the investigation of their impact on the reconstruction and discrimination of different materials. First, a possible detector layout is briefly presented, which allows for the reconstruction of secondary particles and muon tracks within the same setup. Afterward, the detection efficiency, the spatial resolution of the detector, and the spacing between the detection layers are varied as key detector parameters. The impact of these variations on the final reconstruction is measured using multiple metrics, including the position, size, and shape, as well as the reconstructed density of the examined target object.

2. SIMULATION

2.1. Event Generation

The event generation follows the same procedure and simulation settings as in [1]. In summary, a total of 100 million air showers are generated with the *Cosmic-ray Shower Library* (*CRY*) [13], corresponding to an equivalent scanning time of around 30 minutes. The interactions of the air shower and all subsequent particles with matter are simulated with the GEANT4 Monte Carlo simulation toolkit [32, 33].

2.2. Detector Layout

Key aspects of the geometry implementation in [1] are also utilized for this work. A cube made out of water or lead with a size of $1\,\mathrm{m}^3$ is placed as the target object in the middle of the container. Several modifications are made to the detector layout to introduce a more realistic detection performance. While the size and position of the detector planes are kept the same, three layers of a 50 mm thick Vinyltoluene-based plastic scintillator are added as additional detector material [27, 28, 29, 30, 31] to simulate their impact on secondary particle production and interaction. The innermost layers of the plastic scintillator are seamlessly attached to another forming a box-like structure. As the following two scintillator layers in each direction have the same size as the innermost one, the corner regions lack detection material and create a small blind spot for particle detection in these areas. A visualization of this geometry is shown in Figure 1. However, no readout from the scintillator material and no particle identification method are emulated. The type and kinematics of the particles hitting the detection layers are directly retrieved from the truth information taken from the simulation data and by fitting the three points of interaction from the three scintillator layers with a least squares method. A particle is discarded if it hits less than three layers or comes from outside the examined volume.
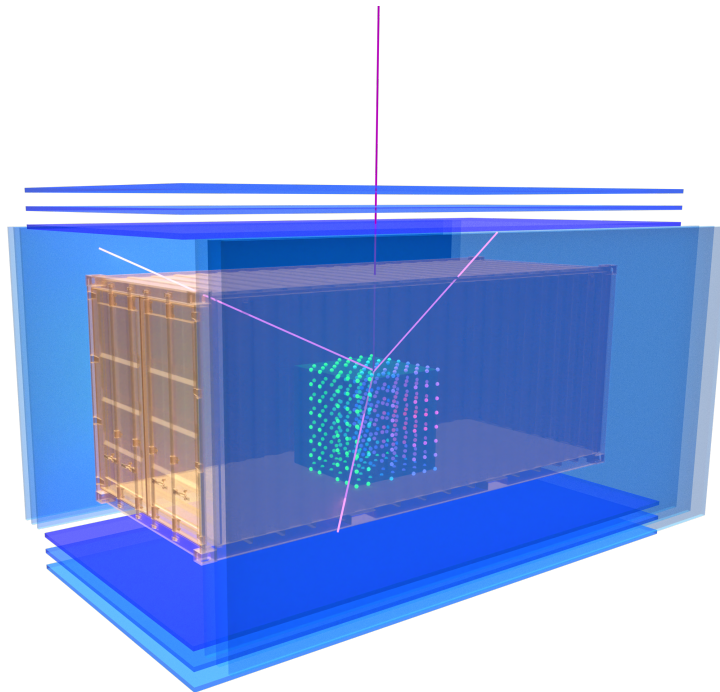
FIGURE 1: A 3D visualization of the detector geometry. The detection planes are shown as the blue layers surrounding the container model. Inside the container, a generic object with its reconstructed density represented by colored dots is depicted. Furthermore, a trajectory of an air shower particle (purple line) with the corresponding secondary particle production (pink lines) is exemplified.

The spacing between the layers is a tunable parameter and is set to either 10 cm or 20 cm. The setup with 10 cm spacing is a design choice suited for a compact detector layout based solely on the analysis of secondary particles. The 20 cm spacing on the other hand allows for an alternating detection setup between detectors dedicated to secondary particles and detectors dedicated to muons. In this case, the additional plastic scintillator layers permit the measurement of the muon momentum to improve the reconstruction of the examined volume through the muon scattering approach [34, 35].

Another tunable parameter is the detection efficiency per layer, which is chosen to be 80%, 60%, or 40%. These values represent realistic efficiencies for photon, neutron, and electron detection over different energies using scintillating materials [36, 37, 38, 39, 40]. The efficiencies are applied by randomly selecting the secondary particle hits with a selection probability being equal to the given efficiency value. The light induced in plastic scintillators is usually collected with a grid of wavelength-shifting (WLS)

fibers. The distance between these fibers determines the spatial resolution of the detector in its horizontal plane. Realistic resolution values are 10 mm, 20 mm, or 30 mm [41, 42, 43]. Furthermore, the realistic 50 mm thickness of the scintillator [44, 45] results in a spatial resolution in the direction perpendicular to the detector plane. These spatial resolutions are applied as the third key detector parameter through Gaussian smearing after the simulation. The exact position of the secondary particle hit is smeared by a normal distribution with the full width at half-maximum set to the spatial resolution values.

3. RECONSTRUCTION

3.1. Methodology

The reconstruction of the examined volume follows the same approach as discussed in [1]. In summary, each detected particle is linearly traced back from the location where it hits the innermost detector through the voxelized volume via ray tracing and each voxel crossed is marked. The more tracks passing through a voxel, the higher its voxel score s_{voxel}, which acts as a representation of the material characteristics, mainly density and atomic number. Hence, the voxel score is also referred to as the density score in the following lines. Afterward, the background of the container is removed by subtracting the voxel map of an empty container, which is based on 1 billion air shower events to reduce the effect of fluctuations in the background correction.

The presented voxel map reconstruction procedure is performed separately for secondary particle type (photon, neutron, electron), each detector layer considered (upper detector, sidewise detector, lower detector), and energy regimes of certain secondary particles. This split results in twelve voxel maps, the so-called measurements $M1$–$M10$, as shown in Table 1.

	Photons	Neutrons	Electrons
Upper detector—production	$M1^{\alpha}$, $M2.1^{\beta}$	$M3$	—
Upper detector—absorption	$M2.2^{\beta}$	—	—
Sidewise detector—production	$M4^{\alpha}$, $M5.1^{\beta}$	$M6$	—
Sidewise detector—absorption	$M5.2^{\beta}$	—	—
Lower detector—production	—	$M8^{\gamma}$	—
Lower detector—absorption	$M7$	$M9^{\delta}$	$M10$

$^{\alpha}$>400 keV, $^{\beta}$<400 keV, $^{\gamma}$<3 MeV, $^{\delta}$>3 MeV

TABLE 1: The separate measurements for the different particle types, their energies, and detector planes. $M2.1$ and $M2.2$, as well as $M5.1$ and $M5.2$, are mutually exclusive.

These measurement definitions are updated compared to [1], as the detected particle kinematics changed due to the additional production and absorption effects of the added scintillation material on secondary particles. Low-energy (below 400 keV) photons detected in the upper and sidewise detectors can now either be used as particle production ($M2.1$ and $M5.1$) or absorption ($M2.2$ and $M5.2$) measurement. The absorption measurements are suitable for high-density test objects, as they will absorb most of the additional low-energy photons produced in the scintillator material, while low-density test objects will absorb only a small fraction of those. During the interaction of the additional low-energy secondary particles with the object material, more low-energy photons are produced. In case of a high-density material, most of these photons are directly absorbed before exiting the test object. However, this is different in low-density test objects, resulting in the detection of more low-energy photons. This makes the production measurements suitable for low-density test objects. It is important to note that $M2.1$ ($M5.1$) and $M2.2$ ($M5.2$) are mutually exclusive. In the lower detector, nearly all of the secondary photons are absorbed by the objects and the multiple layers of the plastic scintillator. Secondary photons are mainly produced in the upper part of the object, which results in more energy loss and a higher chance of absorption of the secondary photon due to the longer path through the object to the lower detector compared to the upper and sidewise layers. In addition, the secondary photons produced at the lower part of the object inherit less energy from their mother air shower particle due to its increased energy loss while passing through the upper part of the object before the photon is produced. This results in a higher absorption rate of secondary photons in the scintillator material of the lower detector compared to the upper and sidewise layers. Therefore, only the photon absorption is a viable measurement in the lower detector. The number of secondary neutrons detected in the lower detector is also small, but not vanishing compared to the photons, and therefore, this measurement is still part of the analysis.

By combining measurements from Table 1, discrimination between materials is possible due to the different kinematics represented by the separate measurements. However, a measurement is only utilized for the combination if it is capable of discriminating the target object against the background noise by itself. To reduce noise and enhance the discrimination, a tunable minimum voxel score threshold t_{min} is applied separately for every selected measurement, with the threshold set relative to the maximum voxel score s_{max} in the given measurement: $s_{\text{voxel}} > s_{\text{max}} * t_{\text{min}}$.

The final combination is done voxel by voxel, by summing the scores of the selected measurements, but only if every measurement fulfills the minimum threshold requirement. As mentioned previously, the examined materials are water and lead. The set of measurements with the thresholds for water and lead is listed in Tables 2 and 3. To ensure a better statistical significance of the reconstruction of the water cube, $M1$ and $M2.1$, as well as $M4$ and $M5.1$, are combined with a single-photon production measurement for the upper and sidewise detectors separately.

	Photons	Neutrons	Electrons
Upper detector—production	20%	—	—
Upper detector—absorption	—	—	—
Sidewise detector—production	30%	—	—
Sidewise detector—absorption	—	—	—
Lower detector—production	—	—	—
Lower detector—absorption	30%	40%	40%

TABLE 2: The separate measurements and the minimum voxel score thresholds for the different particle types and detector planes for the reconstruction of the water cube.

	Photons	Neutrons	Electrons
Upper detector—production	$15\%^{\alpha}, —^{\beta}$	15%	—
Upper detector—absorption	—	—	—
Sidewise detector—production	$25\%^{\alpha}, —^{\beta}$	25%	—
Sidewise detector—absorption	—	—	—
Lower detector—production	—	—	—
Lower detector—absorption	40%	40%	50%

$^{\alpha}>400\,\text{keV}, ^{\beta}<400\,\text{keV}$

TABLE 3: The separate measurements and the minimum voxel score thresholds for the different particle types and detector planes for the reconstruction of the lead cube.

3.2. Performance Metrics

To measure the impact of the different parameters of the more realistic detector setup, a set of metrics needs to be established. However, to ensure that these metrics are consistent and not significantly biased by statistical fluctuations, first, a clustering algorithm is applied to the reconstructed voxel map to evaluate the target cube. This method starts with the voxel with the highest score as the seed, loops over the surrounding voxels, and adds them to the cluster if their density score is at least 80% of the mean cluster score. As we have a single cube as the only object in the examined volume, no additional cluster is calculated. Each reconstructed cluster is then characterized by five performance metrics:

  (i) Mean density score

 (ii) Volume: Sum over all voxels associated with the cluster, where each voxel has a voxel size of $1\,\text{dm}^3$

(iii) Maximum side lengths (d_x, d_y, d_z): Difference between the maximum and minimum x-, y-, or z-positions of the cluster

(iv) Positional shift $(\Delta x_{\text{pos.}}, \Delta y_{\text{pos.}}, \Delta z_{\text{pos.}})$: Difference between the position of the volumetric center of the reconstructed and the ground truth object

 (v) Chamfer distance (d_C): A common metric used in the training of machine learning networks for point cloud identification and discrimination to evaluate the shape difference of two objects [46, 47].
     While there are different definitions of how to calculate the Chamfer distance, the following method is used in this analysis:

    (1) Center the reconstructed voxel cluster and the ground truth voxelized object at the origin
    (2) For each voxel in the reconstructed cluster, measure the squared distance to the nearest voxel of the ground truth object
    (3) Sum the squared distances for all voxels in the reconstructed cluster
    (4) Repeat steps (2) and (3) for all voxels in the ground truth object with the squared distances to the nearest reconstructed voxel
    (5) Calculate the Chamfer distance as the mean between the sum in step (3) and the sum in step (4).

    The value of the Chamfer distance has no absolute meaning and is only used for relative comparison. Usually, a smaller Chamfer distance represents less differences in the shapes of the reconstructed and the ground truth object. However, the Chamfer distance can be biased if one of the probed objects has a significantly smaller volume than the other object, as this reduces the number of voxels and therefore the sum in step (2) or step (4). Therefore, the Chamfer distance proves most valuable when clusters are of a similar size.

4. RESULTS

4.1. Impact of Multiple Layers

As a particle needs to pass through all three scintillator layers to be detected, the new multilayer detector setup has a lower detection probability than a single-layer setup. This inefficiency, the so-called acceptance, can be measured by comparing the mean cluster density score for the single-layer scenario, as described in [1], and the three-layer setup discussed in this work. This is possible as the density score is directly proportional to the number of reconstructed particles in the detectors. The acceptance depends on the particle, its energy, and whether it was measured in the upper, sidewise, or lower detector and is therefore different for each measurement combination. Hence, the acceptance of the optimized measurement of a water block is different from the optimized measurement for a lead cube. To remove any possible effect of the other parameters of the detector setup, the detection efficiency is set to 100% for all particles, and an ideal spatial resolution is assumed. We also assume for the single-layer scenario that all necessary kinematic information to reconstruct the volume can be extracted from one layer only.

A comparison of the performance metrics for the lead cube is shown in Table 4 and for the water cube in Table 5. The reconstructed maps for both materials for the single-layer scenario and the three-layer scenario with 10 cm spacing are shown in Figure 2. The acceptance is calculated as the density score of the 3-layer setup over the 1-layer setup and is very similar for the 10 cm and the 20 cm spacing in the lead object scenario at 32-33%. The water cube case shows a similar result, with an acceptance of 53% in both cases. The higher value in the water scenario can be explained by the fact that the secondary particles produced in water lose less energy while passing through the cube than the ones from the lead block due to the lower density of water. Therefore, the chance of having lower-energy secondary particles absorbed in the plastic scintillators, resulting in a lower acceptance, is higher in the lead than in the water block setup.

	Score	Size	d_x	d_y	d_z	$\Delta x_{\text{pos.}}$	$\Delta y_{\text{pos.}}$	$\Delta z_{\text{pos.}}$	d_C
Ground truth	—	$1.210\,\text{m}^3$	1.1 m	1.0 m	1.1 m	—	—	—	—
1 layer	17829	$0.942\,\text{m}^3$	1.1 m	1.0 m	1.2 m	0.00 m	0.00 m	0.25 m	4.8
3 layers, 10 cm	5896	$1.388\,\text{m}^3$	1.1 m	1.0 m	1.9 m	0.00 m	0.00 m	0.20 m	12.1
3 layers, 20 cm	5668	$1.332\,\text{m}^3$	1.1 m	1.0 m	1.8 m	0.00 m	0.00 m	0.15 m	11.2

TABLE 4: Comparison of the performance metrics for the ground truth and the reconstructed lead cube for the one-layer scenario and the three-layer scenarios with 10 and 20 cm spacing.

	Score	Size	d_x	d_y	d_z	$\Delta x_{\text{pos.}}$	$\Delta y_{\text{pos.}}$	$\Delta z_{\text{pos.}}$	d_C
Ground truth	—	$1.210\,\text{m}^3$	1.1 m	1.0 m	1.1 m	—	—	—	—
1 layer	5182	$1.050\,\text{m}^3$	1.1 m	1.0 m	1.4 m	0.00 m	0.00 m	0.15 m	4.6
3 layers, 10 cm	2762	$1.078\,\text{m}^3$	1.0 m	1.0 m	1.7 m	−0.05 m	0.00 m	0.10 m	6.4
3 layers, 20 cm	2755	$1.066\,\text{m}^3$	1.0 m	1.0 m	1.7 m	−0.05 m	0.00 m	0.10 m	8.0

TABLE 5: Comparison of the performance metrics for the ground truth and the reconstructed water cube for the one-layer scenario and the three-layer scenarios with 10 and 20 cm spacing.

In both scenarios, with the water and the lead block, the reconstructed size in the z-direction is larger than the ground truth volume resulting also in a higher Chamfer distance. This increase is higher in the multiple-layer setup but similar to the 10 and 20 cm spacing. However, the increase is generally smaller for the water cube than for the lead block. This is mainly due to the absorption measurement in the lower detector plane. Since air shower particles predominantly have a low zenith angle, reconstructed objects tend to appear stretched in the z-direction. As a higher density relates to a higher absorption rate, this effect is more pronounced for lead than for water. The difference between one and three layers originates from the relative significance of this absorption measurement. As already discussed in the previous section, the additional scintillator material absorbs a large fraction of the lower-energy secondary particles. Hence, the relative importance of the absorption measurement of higher-energy particles is increasing in the combination step of the reconstruction method. This effect can possibly be reduced by careful tuning of the measurement combination. Therefore, all features of the absorption-based maps will also be enhanced in the final combined map. While in the water scenario, the cube volume is relatively constant, the lead block volume changes more significantly between the different setups and the ground truth cube. The reconstructed lead object in the multiple-layer setup shows a rather significant increase in the volume mostly related to the increase in z-direction. As this increase is lower for the water cube, the change in volume is also lower.

The apparent size of the lead block in the single-layer reconstruction is significantly smaller than all other objects. This is mostly due to the decrease in the density score from high to low values on the z-axis. This gradual decrease is a result of the production measurement map from the upper and sidewise detectors. Air shower particles mostly hit the cube on the top and the upper parts of the sides due to the lower zenith angle. Hence, these regions are more active in producing secondary particles. Furthermore, secondary particles produced inside the block have a higher chance of losing more energy, which results in a higher change of absorption in the material or in the detector layers. Therefore, the production measurements in the upper and sidewise detectors
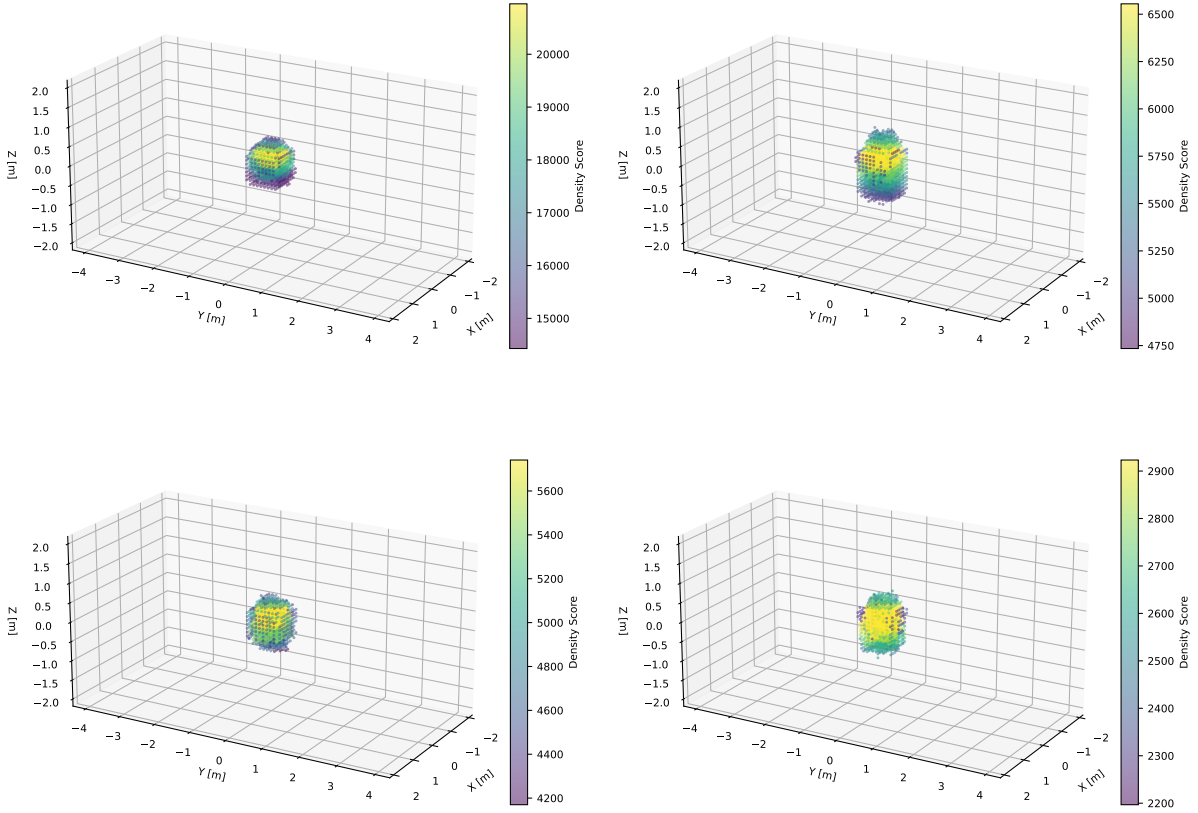
FIGURE 2: The reconstructed lead (top row) and water (bottom row) cubes with their corresponding density scores in the single- (left column) and three-layer scenarios with 10 cm spacing (right column).

show a higher score in the top region of the cube, which also passes to the final combination map. Hence, the reconstructed object is not symmetric with respect to the z-axis and the lower part of the cube is partially chopped away by the clustering. The result is a smaller volume and a slight shift toward a higher z-position. As this effect is more pronounced in higher-density materials due to the different probability of secondary particle production, the resulting features are more visible for lead than for water.

4.2. Impact of Detection Efficiency

For simplicity, the single-layer detection efficiency $\epsilon_{\text{det.}}$ is applied equally to all different particles independently of their energy. Of course, a realistic detection material shows different efficiencies for photons, electrons, and neutrons over the energy spectrum. However, the final reconstruction is mainly driven by the measurement with the lowest statistics due to the requirement in the combination method that a voxel is only kept for the final map if it passes the threshold cut in all selected measurements. The biggest impact of the detection efficiency is a decrease in the effective scanning time, resulting in a lower number of secondary particles and a lower density score measurement $s_{\text{meas.}}$. Therefore, all scores in the efficiency scenarios are corrected to the same effective scan time, which is based on a detection efficiency of 100%: $s_{\text{cor.}} = s_{\text{meas.}}/\epsilon_{\text{det.}}$.[3] To avoid any possible effect of the other detector parameters, an ideal spatial resolution and three layers with a spacing of 10 cm are assumed.

The impact of the detection efficiency on the performance metrics for the lead and water block is shown in Tables 6 and 7. The reconstructed lead and water cubes for 100% and 80% detection efficiency are shown in Figure 3. Both material setups show a clear increase in the corrected density score with lower detection efficiency. With less scan time, only the inner parts of the cube will be present, which show the highest density score as this is directly related to the number of secondary particles. Parts with lower scores will be ignored by the clustering algorithm resulting in a higher mean cluster score. This is also visible in the overall volume of the cube, which gets smaller with lower detection efficiency, affecting the Chamfer distance in a similar way. However, the 40% efficiency scenario is mostly affected by the interplay of low statistics and the measurement combination method. The statistical fluctuation for a single voxel is increasing with lower efficiency; hence, the chance of not passing the threshold and therefore getting discarded in the final combination is higher. This is more pronounced in the z-direction due to the density score behavior along the z-axis explained in the previous subsection.

Efficiency	Score[†]	Size	d_x	d_y	d_z	$\Delta x_{\text{pos.}}$	$\Delta y_{\text{pos.}}$	$\Delta z_{\text{pos.}}$	d_C
100%	5896	$1.388\,\text{m}^3$	$1.1\,\text{m}$	$1.0\,\text{m}$	$1.9\,\text{m}$	$0.00\,\text{m}$	$0.00\,\text{m}$	$0.20\,\text{m}$	12.1
80%	6020	$1.371\,\text{m}^3$	$1.1\,\text{m}$	$1.1\,\text{m}$	$2.0\,\text{m}$	$0.00\,\text{m}$	$0.05\,\text{m}$	$0.15\,\text{m}$	14.1
60%	6475	$1.117\,\text{m}^3$	$1.1\,\text{m}$	$1.1\,\text{m}$	$1.7\,\text{m}$	$0.00\,\text{m}$	$-0.05\,\text{m}$	$0.10\,\text{m}$	5.3
40%	7367	$0.627\,\text{m}^3$	$1.1\,\text{m}$	$1.1\,\text{m}$	$1.6\,\text{m}$	$0.00\,\text{m}$	$-0.05\,\text{m}$	$0.15\,\text{m}$	7.6

[†] Corrected against the loss in effective scan time

TABLE 6: The impact of varying the detection efficiency per layer on the performance metrics for the reconstructed lead cube.

Efficiency	Score[†]	Size	d_x	d_y	d_z	$\Delta x_{\text{pos.}}$	$\Delta y_{\text{pos.}}$	$\Delta z_{\text{pos.}}$	d_C
100%	2762	$1.078\,\text{m}^3$	$1.1\,\text{m}$	$1.0\,\text{m}$	$1.7\,\text{m}$	$-0.05\,\text{m}$	$0.00\,\text{m}$	$0.10\,\text{m}$	6.4
80%	2962	$1.132\,\text{m}^3$	$1.1\,\text{m}$	$1.1\,\text{m}$	$1.2\,\text{m}$	$0.00\,\text{m}$	$0.05\,\text{m}$	$0.15\,\text{m}$	10.9
60%	3255	$1.079\,\text{m}^3$	$1.1\,\text{m}$	$1.0\,\text{m}$	$1.9\,\text{m}$	$0.00\,\text{m}$	$0.00\,\text{m}$	$0.15\,\text{m}$	7.1
40%	3983	$0.551\,\text{m}^3$	$1.1\,\text{m}$	$1.1\,\text{m}$	$1.8\,\text{m}$	$0.00\,\text{m}$	$0.05\,\text{m}$	$0.10\,\text{m}$	7.1

[†] Corrected against the loss in effective scan time

TABLE 7: The impact of varying the detection efficiency per layer on the performance metrics for the reconstructed water cube.
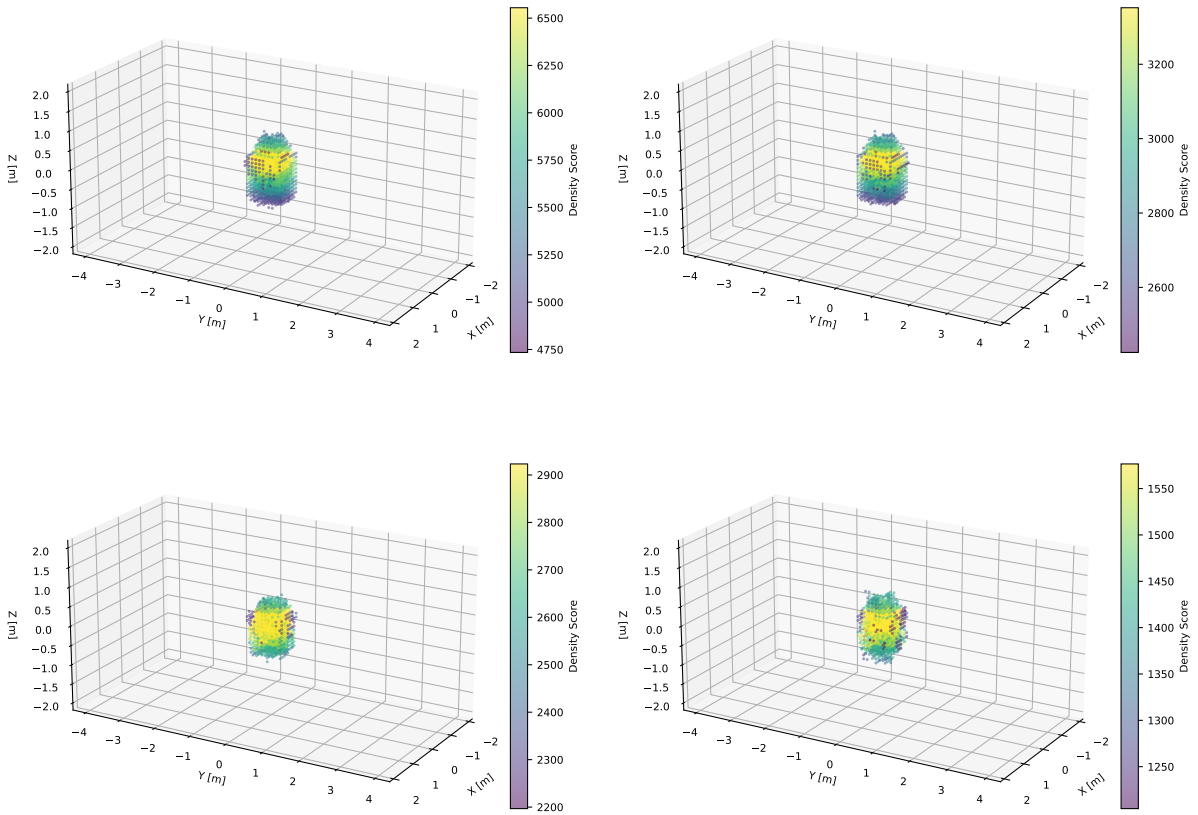
FIGURE 3: The reconstructed lead (top row) and water (bottom row) cubes with their corresponding uncorrected density scores in the 100% (left column) and 50% layer detection efficiency scenario (right column).

4.3. Impact of Detection Resolution

The spatial resolution of the detector consists of two parts, the assumed WLS fiber grid spacing ($10\,\text{mm}$, $20\,\text{mm}$, and $30\,\text{mm}$) and the fixed thickness of the scintillator ($50\,\text{mm}$), resulting in three resolution scenarios: $10{:}50\,\text{mm}$, $20{:}50\,\text{mm}$, and $30{:}50\,\text{mm}$. For simplicity, all particles in all energy regimes are assumed to be detected with the same resolution. This can be justified as the resolution is mostly driven by the detector setup and not by the particle kinematics. To prevent unwanted effects by changing the other detector parameters, the detection efficiency is set to 100% and the spacing between each of the three layers is $10\,\text{cm}$.

The resulting performance metrics for the study of the resolution impact for both material cubes are shown in Tables 8 and 9. Their reconstruction for the ideal and 30:50 mm resolution scenarios is shown in Figure 4. Overall, the density scores shows a reduction with worse detection resolution. Due to the additional resolution, the inner voxels with a high score get smeared with the low score voxels outside the cube and, hence, the mean density score of the cluster drops. While the reconstructed size seems to be similar for the different resolution values, the Chamfer distance shows a tendency to increase with higher resolution values. This can be explained by the change of the object shape due to the smearing effect of the resolution.

Resolution	Score	Size	d_x	d_y	d_z	$\Delta x_{\text{pos.}}$	$\Delta y_{\text{pos.}}$	$\Delta z_{\text{pos.}}$	d_C
Ideal	5896	$1.388\,\text{m}^3$	1.1 m	1.0 m	1.9 m	0.00 m	0.00 m	0.20 m	12.1
10:50 mm	5726	$1.357\,\text{m}^3$	1.0 m	1.0 m	2.0 m	0.05 m	0.00 m	0.15 m	16.3
20:50 mm	5573	$1.352\,\text{m}^3$	1.0 m	1.0 m	2.0 m	0.05 m	0.00 m	0.15 m	17.7
30:50 mm	5266	$1.419\,\text{m}^3$	1.2 m	1.2 m	1.9 m	-0.05 m	0.00 m	0.10 m	11.5

TABLE 8: The impact of varying the detection resolution on the performance metrics for the reconstructed lead cube.

Resolution	Score	Size	d_x	d_y	d_z	$\Delta x_{\text{pos.}}$	$\Delta y_{\text{pos.}}$	$\Delta z_{\text{pos.}}$	d_C
Ideal	2762	$1.078\,\text{m}^3$	1.1 m	1.0 m	1.7 m	-0.05 m	0.00 m	0.10 m	6.4
10:50 mm	2697	$1.053\,\text{m}^3$	1.1 m	1.0 m	1.7 m	0.00 m	0.00 m	0.10 m	5.6
20:50 mm	2640	$0.988\,\text{m}^3$	0.9 m	1.0 m	2.0 m	0.00 m	0.00 m	0.15 m	9.5
30:50 mm	2505	$1.050\,\text{m}^3$	1.1 m	1.0 m	1.8 m	0.00 m	0.00 m	0.15 m	10.7

TABLE 9: The impact of varying the detection resolution on the performance metrics for the reconstructed water cube.
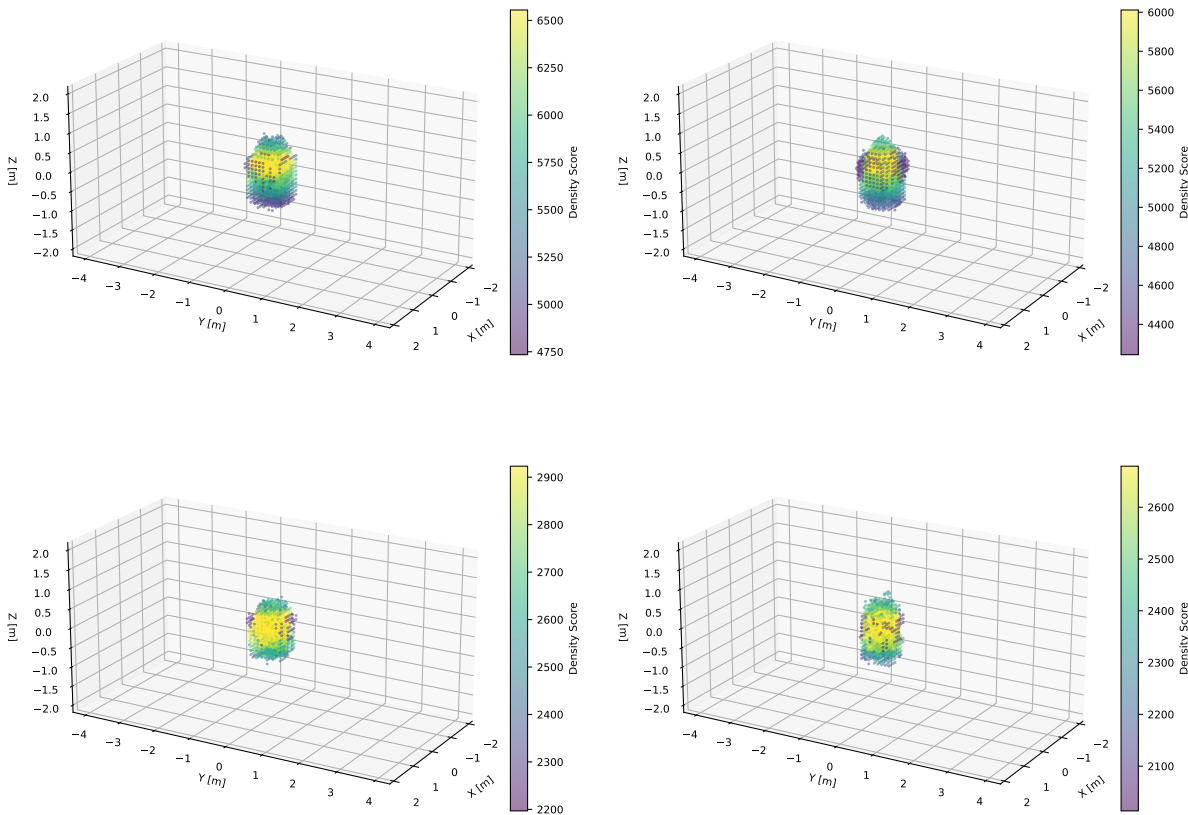
FIGURE 4: The reconstructed lead (top row) and water (bottom row) cubes with their corresponding density scores in the ideal (left column) and 30:50 mm resolution scenario (right column).

4.4. Impact of Layer Spacing

To assess the difference between the two layer spacing setups, the ratio of the 10 cm over the 20 cm spacing is calculated for the reconstructed density score volume for the different efficiency and resolution parameter values. This is done for the lead and the water cube scenario, and the results are shown in Table 10. Overall, the difference between the two spacing scenarios is small. Both materials show a small relation between the ratio of the density scores and the resolution, as the ratio decreases with worsening resolution values. This is expected as the smearing of the object for a fixed spatial resolution decreases with increasing distance between the layers. The water cube also shows an increasing size ratio for decreasing efficiency. However, as this trend is not visible for the lead block and the statistics for the 60% and especially 40% efficiency scenario are low, currently, no statement about this correlation can be made.

Efficiency	Lead score	Lead size	Water score	Water size
100%	1.040	1.042	1.003	1.011
80%	1.039	1.011	1.014	1.154
60%	1.066	0.882	1.020	1.255
40%	1.040	1.161	1.017	1.611
Resolution	Lead score	Lead size	Water score	Water size
Ideal	1.040	1.042	1.003	1.011
10:50 mm	1.020	0.996	0.996	1.021
20:50 mm	1.007	0.988	0.961	1.035
30:50 mm	0.967	1.065	0.926	1.087

TABLE 10: The ratio of the 10 cm over the 20 cm layer spacing setup for the reconstructed density score and volume of the lead and water block for the efficiency and resolution parameter values.

4.5. Impact on Material Discrimination

Under the assumptions of this work, the impact of more realistic detection efficiency and resolution on the discrimination between the lead and water material is studied. This is done by calculating the ratio of the lead and water cube scenarios for the density score and the volume, for both layer spacing setups. The ratios are shown in Table 11. In general, only small differences are visible for the efficiency and resolution variations resulting in a possible and stable material discrimination for these realistic parameter values. The most visible, but nonetheless small correlation is seen for the score ratio against the efficiency. With decreasing efficiency, the difference between the lead and water score is also decreasing. This can also be seen in Tables 6 and 7, where the relative increase of the score for lower efficiency is larger for the water block. This is a result of the fixed clustering threshold (80%) for both materials. Due to the higher density of lead, the maximum allowed absolute score difference between the cluster and a neighboring voxel is larger than for the water cube with lower density. Hence, more voxels with lower scores can be added to the lead cluster than to the water one. This effect gets amplified for lower efficiency values as the mean cluster score increases resulting in an even higher maximum score difference. The increasing trend seen in the size ratio for decreasing efficiency for the 20 cm spacing has already been discussed in the previous subsection.

Efficiency	Score (10 cm)	Size (10 cm)	Score (20 cm)	Size (20 cm)
100%	2.135	1.288	2.057	1.250
80%	2.032	1.211	1.983	1.382
60%	1.989	1.035	1.904	1.473
40%	1.849	1.138	1.809	1.579
Resolution	Score (10 cm)	Size (10 cm)	Score (20 cm)	Size (20 cm)
Ideal	2.135	1.288	2.057	1.250
10:50 mm	2.123	1.289	2.072	1.322
20:50 mm	2.111	1.368	2.016	1.434
30:50 mm	2.102	1.351	2.013	1.379

TABLE 11: The ratio of the lead over the water cube scenario for the reconstructed density score and volume of the 10 and 20 cm spacing setups for the efficiency and resolution parameter values.

5. DISCUSSION

The usage of secondary particles for cosmic-ray tomography applications provides a promising and complementary approach to improve the results from muon transmission and scattering measurements. This analysis proved that this statement still holds not only for ideal but also for more realistic detector conditions, including the simulation of additional detection material budget and of

common spatial resolution and detector efficiency parameters. The proposed stand-alone method is able to successfully reconstruct simple geometric objects, which are located inside a container, and to discriminate their material for the various simulated detector conditions. The impact of the additional material mostly results in an adaption of the measurement set for the reconstruction procedure due to a change in particle kinematics, especially for low-energy particles, and a longer scan time due to the system acceptance. The biggest impact due to the realistic detection efficiency is a loss in effective scan time and therefore a higher influence of statistical fluctuations. The spatial resolution has a only minor impact on the reconstructed object, mostly resulting in a small degradation of the reconstructed density score. The difference between the two layer spacing setups is negligible and allows for better flexibility of a potential secondary particle and muon detection system.

The future work will focus on the improvement of the detector setup making it even more realistic by considering a wider range of potential detector materials and more complex target objects. Furthermore, planned improvements on the analysis chain include the implementation of a machine-learning-based reconstruction method, a combination with the result of the muon measurement, and an automized material parameter scan to optimize density and object discrimination.

CONFLICTS OF INTEREST

The authors declare no conflicts of interest. The funders had no role in the design of the study; in the collection, analyses, or interpretation of data; in the writing of the manuscript; or in the decision to publish the results.

ACKNOWLEDGMENTS

References

[1] Pérez Prada, M., Barnes, S., Stephan, M. Analysis of Secondary Particles as a Complement to Muon Scattering Measurements. *Instruments* **2022**, *6*.

[2] Morishima, K., Kuno, M., Nishio, A., Kitagawa, N., Manabe, Y., Moto, M., Takasaki, F., Fujii, H., Satoh, K., Kodama, H., et al. Discovery of a big void in Khufu's Pyramid by observation of cosmic-ray muons. *Nature* **2017**, *552*, 386–390.

[3] Marteau, J., de Bremond d'Ars, J., Gibert, D., Jourde, K., Ianigro, J. C., Carlus, B. DIAPHANE: Muon tomography applied to volcanoes, civil engineering, archaelogy. *J. Instrum.* **2017**, *12*, C02008.

[4] Borozdin, K., Greene, S., Lukić, Z., Milner, E., Miyadera, H., Morris, C., Perry, J. Cosmic ray radiography of the damaged cores of the Fukushima reactors. *Phys. Rev. Lett.* **2012**, *109*, 152501.

[5] Clarkson, A., Ireland, D. G., Al Jebali, R., Kaiser, R., Lumsden, S., Mahon, D., Mountford, D., Ryan, M., Shearer, C., Yang, G. Characterising encapsulated nuclear waste using cosmic-ray Muon Tomography (MT). In Proceedings of the 2015 4th International Conference on Advancements in Nuclear Instrumentation Measurement Methods and Their Applications (ANIMMA), Lisbon, Portugal, 20–24 April 2015, pp. 1–7.

[6] Tanaka, H. K., Taira, H., Uchida, T., Tanaka, M., Takeo, M., Ohminato, T., Aoki, Y., Nishitama, R., Shoji, D., Tsuiji, H. Three-dimensional computational axial tomography scan of a volcano with cosmic ray muon radiography. *J. Geophys. Res. Solid Earth* **2010**, *115*.

[7] Fehr, F. and the TOMUVOL Collaboration. Density imaging of volcanos with atmospheric muons. In *Proceedings of the Journal of Physics: Conference Series*, IOP Publishing: Bristol, UK, 2012, Volume 375, p. 052019.

[8] Armitage, J., Botte, J., Boudjemline, K., Erlandson, A., Robichaud, A., Bueno, J., Bryman, D., Gazit, R., Hydomako, R., Liu, Z., et al. First images from the cript muon tomography system. In *Proceedings of the International Journal of Modern Physics: Conference Series*, World Scientific: Singapur, Singapur, 2014, Volume 27, p. 1460129.

[9] Barnes, S., Georgadze, A., Giammanco, A., Kiisk, M., Kudryavstev, V., Lagrange, M., Pinto, O. L., Cosmic-Ray Tomography for Border Security. *Instruments* **2023**, *7*.

[10] Greisen, K. Cosmic ray showers. *Annu. Rev. Nucl. Sci.* **1960**, *10*, 63–108.

[11] Gaisser, T. K., Engel, R., Resconi, E. Cosmic Rays and Particle Physics. Cambridge University Press: Cambridge, UK, 2016.

[12] Heck, D., Knapp, J., Capdevielle, J., Schatz, G., Thouw, T. CORSIKA: A Monte Carlo code to simulate extensive air showers. *Rep. Fzka* **1998**, *6019*.

[13] Hagmann, C., Lange, D., Wright, D. Cosmic-ray shower generator (CRY) for Monte Carlo transport codes. In Proceedings of the 2007 IEEE Nuclear Science Symposium Conference Record, Honolulu, USA, 26 October–3 November 2007, Volume 2, pp. 1143–1146.

[14] Schultz, L. J., Blanpied, G. S., Borozdin, K. N., Fraser, A. M., Hengartner, N. W., Klimenko, A. V., Morris, C. L., Orum, C., Sossong, M. J. Statistical reconstruction for cosmic ray muon tomography. *IEEE Trans. Image Process.* **2007**, *16*, 1985–1993.

[15] Barnes, S., Stephan, M., Sill Torres, F., Gabriel, A., Wrede, C. P., Wendt, N. S., Nickel, V. The COSMICS (Container Scanning by Muon-based Imaging using Cosmic rayS) Project, an introduction and preliminary results. In Proceedings of the MARESEC 2021, Virtual, 14 June 2021.

[16] Saracino, G., Ambrosino, F., Bonechi, L., Cimmino, L., D'Alessandro, R., D'Errico, M., Noli, P., Scognamiglio, L., Strolin, P. Applications of muon absorption radiography to the fields of archaeology and civil engineering. *Philos. Trans. R. Soc. A* **2019**, *377*, 20180057.

[17] Carbone, D., Gibert, D., Marteau, J., Diament, M., Zuccarello, L., Galichet, E. An experiment of muon radiography at Mt Etna (Italy). *Geophys. J. Int.* **2014**, *196*, 633–643.

[18] Perkins, D. H. Introduction to High Energy Physics. Cambridge University Press: Cambridge, UK, 2000.

[19] Martin, B. R., Shaw, G. Particle Physics. John Wiley & Sons: Hoboken, USA, 2017.

[20] Cottingham, W. N., Greenwood, D. A. An Introduction to Nuclear Physics. Cambridge University Press: Cambridge, UK, 2001.

[21] Blackwell, T., Kudryavtsev, V. Development of a 3D muon disappearance algorithm for muon scattering tomography. *J. Instrum.* **2015**, *10*, T05006.

[22] Tanabashi, M., Hagiwara, K., Hikasa, K., Nakamura, K., Sumino, Y., Takahashi, F., Tanaka, J., Agashe, K., Aielli, G., Amsler, C., et al. Review of particle physics. *Phys. Rev. D* **2018**, *98*, 030001.

[23] Ferrari, A., Sala, P. R. The Physics of High Energy Reactions. Technical Report, CERN-ATL-PHYS-97-113, Available online: https://cds.cern.ch/record/682497 (accessed on 27 September 2023).

[24] Leo, W. R. Techniques for Nuclear and Particle Physics Experiments: A How-to Approach. Springer Science & Business Media: Berlin/Heidelberg, Germany, 2012.

[25] Stein, P., Odian, A., Wattenberg, A., Weinstein, R. Dependence on atomic number of the nuclear photoeffect at high energies. *Phys. Rev.* **1960**, *119*, 348.

[26] Bikit, I., Mrdja, D., Bikit, K., Slivka, J., Jovancevic, N., Oláh, L., Hamar, G., Varga, D. Novel approach to imaging by cosmic-ray muons. *Europhys. Lett.* **2016**, *113*, 58001.

[27] Galgóczi, G., Mrdja, D., Bikit, I., Bikit, K., Slivka, J., Hansman, J., Oláh, L., Hamar, G., Varga, D. Imaging by muons and their induced secondary particles—A novel technique. *J. Instrum.* **2020**, *15*, C06014.

[28] Bacon, J. D., Borozdin, K. N., Fabritius, I., Joseph, M., Morris, C., Perry, J. O. Muon Induced Fission Neutrons in Coincidence with Muon Tomography, Technical Report, Los Alamos National Lab: Los Alamos, USA, 2013.

[29] Borozdin, K. N., Morris, C., Klimenko, A. V., Spaulding, R., Bacon, J. Passive imaging of SNM with cosmic-ray generated neutrons and gamma-rays. In Proceedings of the IEEE Nuclear Science Symposuim & Medical Imaging Conference, Knoxville, USA, 30 October–6 November 2010, pp. 3864–3867.

[30] Luo, S. Y., Huang, Y. H., Ji, X. T., He, L., Xiao, W. C., Luo, F. J., Feng, S., Xiao, M., Wang, X. D. Hybrid model for muon tomography and quantitative analysis of image quality. *Nucl. Sci. Tech.* **2022**, *33*.

[31] Blackwell, T. B. The Use of Cosmic-Rays in Detecting Illicit Nuclear Materials. Ph.D. Thesis, University of Sheffield, Sheffield, UK, 2015.

[32] Agostinelli, S., Allison, J., Amako, K., Apostolakis, J., Araujo, H., Arce, P., Asai, M., Axen, D., Banerjee, S., Barrand, G., et al. GEANT4—A simulation toolkit. *Nucl. Instruments Methods Phys. Res. Sect. A Accel. Spectrometers Detect. Assoc. Equip.* **2003**, *506*, 250–303.

[33] Koi, T. A Geant4 physics list for shielding calculation. In Proceedings of the Shielding Aspects of Accelerators, Targets and Irradiation Facilities–SATIF10, Geneva, Switzerland, 2–4 June 201, pp. 407–412.

[34] Bae, J., Chatzidakis, S. Momentum-Dependent Cosmic Ray Muon Computed Tomography Using a Fieldable Muon Spectrometer. *Energies* **2022**, *15*.

[35] Anghel, V., Armitage, J., Baig, F., et al. A plastic scintillator-based muon tomography system with an integrated muon spectrometer. *Nucl. Instruments Methods Phys. Res. Sect. A Accel. Spectrometers Detect. Assoc. Equip.* **2015**, *798*, 12–23.

[36] Neupane, S., Heideman, J., Grzywacz, R., Hooker, J., Jones, K. L., Kitamura, N., Thornsberry, C. R., Heilbronn, L. H., Rajabali, M. M., Alberty-Jones, Y., Derkin, J., Massey, T. N., Soltesz, D. Neutron detection efficiency of the Neutron dEtector with Xn Tracking (NEXT). *Nucl. Instruments Methods Phys. Res. Sect. A Accel. Spectrometers Detect. Assoc. Equip.* **2021**, *1020*, 165881.

[37] Baumann, T. Design of a neutron detector. Project Report, National Superconducting Cyclotron Laboratory: East Lansing, USA, 2001.

[38] Sharma, S., Baran, J., Chug, N., et al. Efficiency determination of J-PET: first plastic scintillators-based PET scanner. *European Journal of Nuclear Medicine and Molecular Imaging* **2023**, *10*, 165881.

[39] Chiba, M., Fukunaga, C., Wada, T., Nakagawa, Y., Kobayashi, M., Kurokawa, S. I., Koike, M., Omori, T., Fujitani, T. Performance of a scintillator glass calorimeter for 10.1–84.3 MeV photons. *Nucl. Instruments Methods Phys. Res. Sect. A Accel. Spectrometers Detect. Assoc. Equip.* **1985**, *234*, 267–270.

[40] Pourtangestani, K. Optimization of Plastic Scintillator Thicknesses for Online Beta Detection in Mixed Fields. M.Sc. Thesis, University of Ontario Institute of Technology, Oshawa, Canada, 2010.

[41] Jo, W. J., Kim, H. I., An, S. J., Lee, C. Y., Baek, C. H., Chung, Y. H. Design of a muon tomography system with a plastic scintillator and wavelength-shifting fiber arrays. *Nucl. Instruments Methods Phys. Res. Sect. A Accel. Spectrometers Detect. Assoc. Equip.* **2013**, *732*, 568–572.

[42] Dong, J. N., Zhang, Y. L., Zhang, Z. Y., Liu, D., Xu, Z. Z., Wang, X. L., Liu, S. B. Position-sensitive plastic scintillator detector with WLS-fiber readout. *Nucl. Sci. Tech.* **2018**, *29*.

[43] Jie, H., Yafei, Q., Haiyan, L., Lihua, R., Yantao, Q., Wei, W., Ying, W., Xia, L., Zhiping, L., Jizeng, M. Optimisation and performance test of fibre-based large-area surface contamination monitor. *Results in Physics* **2019**, *15*, 102727.

[44] Mrdja, D., Bikit, I., Bikit, K., Slivka, J., Hansman, J., Oláh, L., Varga, D. First cosmic-ray images of bone and soft tissue. *Europhys. Lett.* **2016**, *116*, 48003.

[45] Ji, X. T., Luo, S. Y., Huang, Y. H., Zhu, K., Zhu, J., Peng, X. Y., Xiao, M., Wang, X. D. A novel 4D resolution imaging method for low and medium atomic number objects at the centimeter scale by coincidence detection technique of cosmic-ray muon and its secondary particles. *Nucl. Sci. Tech.* **2022**, *33*.

[46] Barrow, H. G., Tenenbaum, J. M., Bolles, R. C., Wolf, H. C. Parametric correspondence and chamfer matching: Two new techniques for image matching. In Proceedings of the 5th International Joint Conference on Artificial Intelligence, Cambridge, USA, 22–25 August 1977, pp. 659–663.

[47] Ma, T., Yang, X., Latecki, J. L. Boosting Chamfer Matching by Learning Chamfer Distance Normalization. In Proceedings of the 11th European Conference on Computer Vision, Heraklion, Greece, 5–11 September 2010, pp. 450–463.